Observation of Phase Objects using STEM - Differential Phase Contrast (DPC) Microscopy

Akimitsu Ishizuka, Kazuo Ishizuka

HREM Research Inc.

Scanning transmission electron microscopy (STEM) becomes popular owing to its compatibility with analytical capability. However, it is difficult to observe a phase object using STEM. The differential phase contrast (DPC) microscopy has been proposed to overcome this limitation. Here, a detector is split into two halves, and an image signal (the DPC signal) is given by a difference between the signals from two segments. The split detector has been used to observe a magnetic structure at a low/medium magnification. On the other hand, it has recently been shown that the DPC signals with atomic resolution can be obtained using a multiple quadrant detector. Since it has been demonstrated that the DPC signal is a derivative of phase distribution function of an exit wave, the phase distribution can be restored by integrating the DPC signal. In this report, we introduce the discrete cosine transform (DCT) to integrate the DPC signals for obtaining the phase distribution, because the DCT is consistent with the Neumann boundary condition that is applicable to the data observed only in a finite region. In addition, we describe the real-time integration method that displays the phase distribution in accord with STEM scanning. After that, using the model structure we compare the phase distributions restored by the DCT and the method based on fast Fourier transform (FFT). Then, using experimental data obtained from single-layer graphene we will discuss on observation of phase objects in atomic resolution.

Introduction

The materials act as a phase object for an electron beam, and a high-resolution image observed by transmission electron microscopy (TEM) reflects a phase modulated by the object. For a thin sample, this phase modulation is proportional to the electrostatic potential of the sample, which is approximately proportional to the atomic number. Therefore, the phase contrast image obtained by TEM is important for analyzing the atomic structure of the sample. In recent years, scanning transmission electron microscopy (STEM) has become remarkably popular owing to its compatibility with analysis capabilities, such as electron energy loss spectroscopy. Especially, STEM is particularly effective in analyzing atomic structures in conjunction with aberration correction technology. In high-angle annular dark-field (HAADF) images obtained by STEM, heavy elements can be selectively detected, since image contrast is approximately proportional to the square of the atomic number. However, this means that HAADF images are not suitable to detect light elements. Recently, the annular bright-field (ABF) STEM [1] that can detect light elements has been proposed, but its contrast does not directly represent a phase change as observed by TEM. From the reciprocity theorem the bright-field method in STEM using a small disc-shaped detector, as shown in **Fig. 1** (a), makes it possible to obtain a phase contrast image equivalent to that in TEM. However, the imaging efficiency of this bright-field STEM is extremely poor compared with the one for the phase contrast in TEM, since only a part of incident electrons that hit the small detector contribute to the image formation.

Dekkers and de Lang [2] proposed differential phase contrast (DPC) microscopy to observe a phase object in STEM, where all transmitted electrons are collected by a split detector as shown in Fig. 1 (a), and the difference signal between the outputs from two segments is used to create an image. They demonstrated that using a scanning optical microscope, a phase change perpendicular to the bisector of the detector can be observed. Later, Waddell and Chapman [3] showed that the centroid (center of mass) of the electron diffraction intensity is proportional to a gradient of the phase distribution function. They also showed that the difference signal from the split detector closely approximates the component of the centroid perpendicular to the bisector. Then, if we use a four-segment (quadrant) detector [4] as shown in Fig. 1 (b), without rotating the split detector, approximate differentials of the phase distribution in two perpendicular directions can be obtained simultaneously with a single beam scan. Recently, it has been shown that the DPC signals with atomic resolution can be obtained using multiple quadrant detectors [5]. Now, an eight-segment (double-quadrant) detector and an annular four-segment detector as shown in Figs. 1 (c) and (d), respectively, have been made commercially available. It should be noted here the phase

〉〉 14-48 Matsukazedai, Higashimatsuyama, Saitama 355-0055, Japan | E-mail: ishizuka@hremresearch.com

distribution can be obtained by integrating the DPC signal, since the DPC signal is a gradient of the phase distribution function. Therefore, DPC in STEM (STEM-DPC) not only allows us to detect a phase object, but also gives us an electrostatic potential of a sample that is important for analysis of a sample structure, by integrating the DPC signal.

On the other hand, the propagation direction of electrons is changed by Lorentz force of an electro-magnetic field, which gives contrast of Lorentz microscopy image in TEM. Similarly, Chapman et al. [6] showed that electro-magnetic fields could be observed, if the displacement of the transmission disk when the electron beam passes through the sample is detected by a split detector at each scanning point of the STEM. A recent study of magnetic field observation with an aberration-corrected STEM was discussed by a group at Glasgow University in JEOL News [7].

In recent years, a high-speed pixelated detector (Fig. 1 (e)) that measures diffraction intensity distribution from each scanning point is getting closer to practical use. In this case, since two-dimensional diffraction intensity is obtained for each two-dimensional scanning point, the four-dimensional 4D-STEM data is obtained. Then, a highly accurate DPC signal can be obtained from the centroid of the diffraction intensity distribution of the 4D-STEM data. By using this DPC signal, it is also possible to obtain the phase distribution in quasi-real-time.

In this report we firstly describe the integration methods for obtaining the phase distribution from the DPC signal, and then introduce the qDPC [8], a DigitalMicrograph® plug-in, to which the described integration methods are implemented. In addition, we mention the SD module that directly captures signals from a segmented detector into DigitalMicrograph® and performs phase integration in real time, and also the 4D-STEM module that performs quasi-real-time phase integration from 4D-STEM data obtained by a pixelated detector. Then, we apply DPC integration to an experimental 4D-STEM data obtained from single-layer graphene. Finally, we compare the phase distribution obtained by Ptychography [9] with the phase distribution obtained by integrating the DPC signal.

Integration of the DPC signal

As described above, the DPC signal is the gradient of a phase distribution function, i.e., differential of the phase distribution in two orthogonal directions. Therefore, a phase distribution can be restored by integrating the DPC signal. For this purpose, the following Fourier transform relationship may be used:

$$\partial f(x,y)/\partial x \Leftrightarrow 2\pi i k_x \hat{f}(k_x,k_x) \tag{1}$$

Here, $\hat{f}(k_x,k_x)$ is a Fourier transform of $f(x,y)$, and can be efficiently calculated by using a fast Fourier transform (FFT). When integrating the DPC signal using the Fourier transform, a solution that simultaneously satisfies the two DPC signals, $I_x(x,y)$ and $I_y(x,y)$, should be searched. Among any linear combinations, Close et al. [10] multiplied one of the DPC signals by an imaginary unit i (we call this method FFT-1):

$$\begin{aligned} &I_x(x,y) + iI_y(x,y) = \partial\phi(x,y)/\partial x + i\,\partial\phi(x,y)/\partial y \\ &\Leftrightarrow \hat{I}_x(x,y) + i\hat{I}_y(x,y) = \left(2\pi i k_x - 2\pi k_y\right)\hat{\phi}(k_x,k_x) \end{aligned} \tag{2}$$

On the other hand, a Poisson equation for the phase distribution $\phi(x,y)$ can be obtained when we differentiate the two DPC signals and add them together:

$$\begin{aligned} &\partial I_x(x,y)/\partial x + \partial I_y(x,y)/\partial y = \partial^2\phi(x,y)/\partial x^2 + \partial^2\phi(x,y)/\partial y^2 = \nabla^2\phi \\ &\Leftrightarrow 2\pi i k_x \hat{I}_x(x,y) + 2\pi i k_y \hat{I}_y(x,y) = \left\{(2\pi i k_x)^2 + \left(2\pi i k_y\right)^2\right\}\hat{\phi}(k_x,k_x) \end{aligned} \tag{3}$$

In general, it is necessary to assume a boundary conditions to solve a Poisson equation. Lazic et al. [11] proposed a method using an FFT that assumes periodic boundary conditions (we call this method FFT-2). It may be noted here that we observe the DPC signal that is the derivative of the function to be obtained. Therefore, it should be better to use the Neumann boundary condition that assumes the derivative at the boundary. Then, the discrete cosine transform (DCT) can be used to solve the Poisson equation under Neumann boundary conditions [12].

$$(\lambda_k + \lambda_l) DCT[\phi(i,j)] = DCT[\partial^2\phi(i,j)/\partial x^2 + \partial^2\phi(i,j)/\partial y^2]\Delta^2 \tag{4}$$

Here, DCT indicates the discrete cosine transform, and $\lambda_k = 2\cos(k\pi/m) - 2$. We have implemented the DCT-based solution for integrating the DPC signal to the qDPC [13].

Now, we show the superiority of the DCT solution to the FFT solutions using a synthetic model. **Figure 2** (a) shows the model distribution, and Figs. 2 (b) and (c) show the differences (DPCx, DPCy) of the model distribution in two directions as

Fig. 1 Schematic diagram for differential phase contrast (DPC)

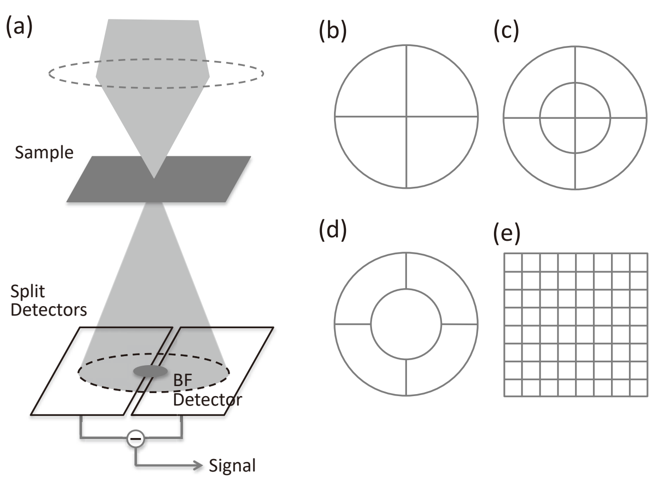

In DPC, all transmitted electrons are detected by a split detector as shown in (a). Using the difference signal between two segments the structure of a phase object that changes perpendicular to the bisector is observed. By using a four-segment detector as shown in (b), it is possible to measure orthogonal DPC signals in two directions simultaneously with a single beam scan. (c) and (d) show a double quadrant (eight-segment) and annular quadrant detectors, respectively, which are commercially available. (e) illustrates schematically a pixelated detector, in which more pixels actually exist.

an approximation of the derivative. Then, we added a random noise of ± 10% of the data range to these differences as shown in (d) and (e), which were used as the model of observed DPC signals. A reconstructed model distribution obtained by integrating the noise added DPCx and DPCy using the DCT is shown in **Fig. 3** (a). For comparison, model distributions obtained by using two FFT methods are shown in Fig. 3 (b) and (c). In the lower part of Fig 3, (d) to (f), show the error in each reconstruction from the model distribution. You may note that in the reconstructions with the FFT there are gradual fluctuations originated from inappropriate periodic boundary conditions. In contrast, the reconstruction with the DCT that employs the Neumann conditions using the differential at the boundary, does not show any appreciable deviation from the model. For this reason, the error in the reconstruction with the DCT is displayed after multiplied by 10, which shows fluctuation equivalent to the random noise added to the signal. We may note here that the results obtained by the DCT as well as two FFTs are smooth, which means the influence of random noise added to the DPC signal is mostly suppressed. As will be described later, using this observation, we can obtain a noise suppressed electric / magnetic field by differentiating the restored phase distribution obtained by integrating an experimental DPC signal.

The integration method described above can be applied only after the whole data are collected at the end of scanning. However, the DPC signals can be progressively displayed according to scanning as other STEM signals. When the phase distribution is displayed in live mode, the throughput of experiment will be significantly improved. If there is no noise in

Fig. 2 Model for evaluating the integration method

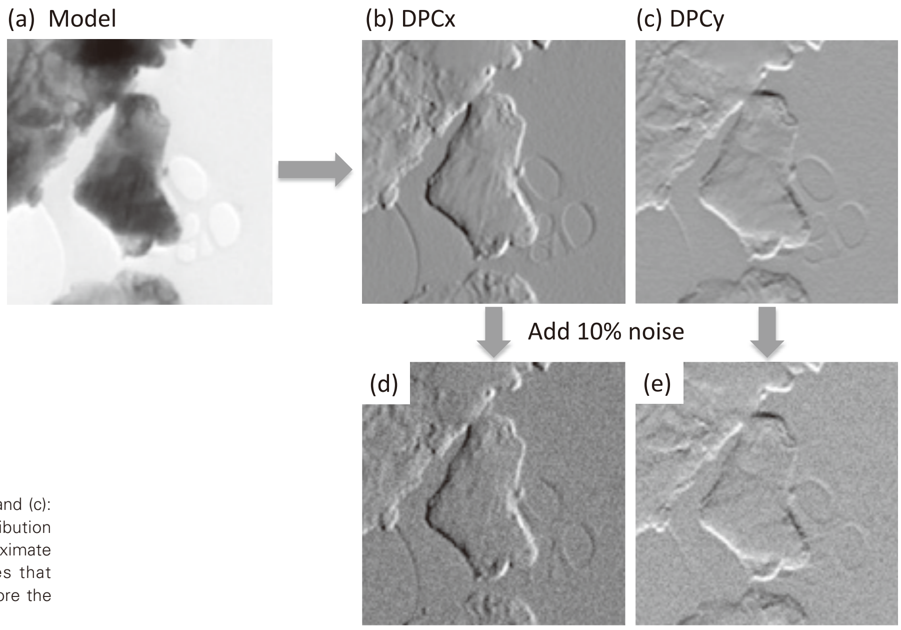

(a): Model distribution function (256 × 256 pixels). (b) and (c): Ideal DPC signals, namely differences of model distribution function along two perpendicular directions that approximate the derivatives. (d) and (e): Noise added derivatives that emulate experiment DPC signals. We attempt to restore the model function from the noise added derivative.

Fig. 3 Phase distributions restored by integration

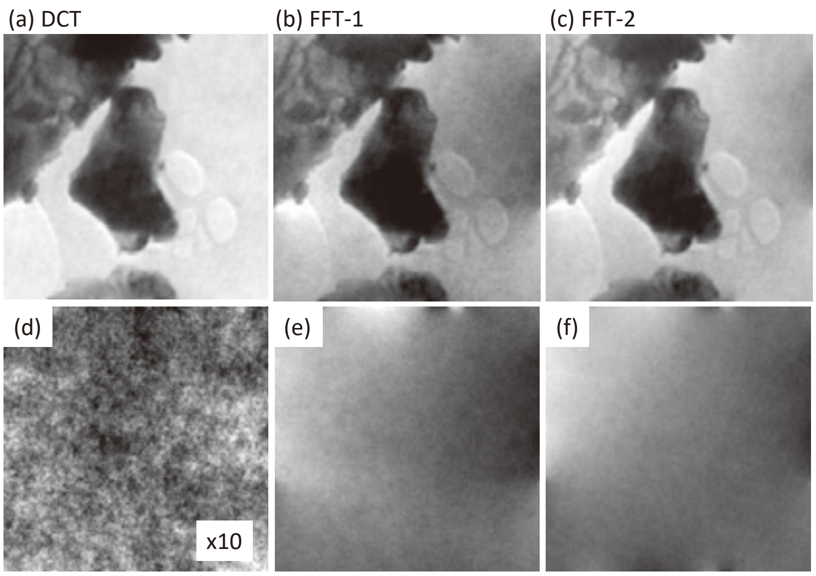

(a): Phase distribution restored by discrete cosine transform (DCT). (b) and (c): Phase distributions restored by two fast Fourier transforms, FFT-1 and FFT-2, respectively. Errors of the reconstructed phase distributions from the model function are shown in (d) to (f), respectively. Since the phase distribution reconstructed by DCT is very close to the model function, the error (d) is displayed after multiplied by 10. On the other hand, the phase distributions restored by the two FFTs show additional slow variations, which result from the failure of the periodic boundary condition.

the DPC signal, a phase distribution may be obtained by simply adding the DPC signals sequentially in the scanning direction. However, there is no experimental data without noise. When we simply add the noise-added DPC signals, shown in Fig. 2, in the horizontal direction, the pronounced horizontal stripes become visible as shown in **Fig. 4** (a). Here, the relationship between the horizontal scan lines is determined by adding the leftmost vertical DPC signal. In contrast, we can obtain Fig. 4 (b), when we estimate the value of the new scanning point from the average of the two derivatives (DPC signals) at the point directly above and the point immediately before. The reconstructed phase is considerably improved compared to (a), although a slowly varying faint pattern appears from top-left to bottom-right. This encourages us to use more the DPC signals to estimate the phase at a new scanning point of interest. Here, we use the fact that all points on the preceding scan line have been already integrated and thus their values have been determined, and that all derivatives on the current scan line are known. Then, using a set of horizontal derivatives on the left and right of the scanning point of interest and a set of vertical derivatives between the previous and current scanning lines, we estimate an integrated value of the said scanning point by the least square method [13]. In Fig. 4 (c), the phase value of the scanning point is determined from the four horizontal and five vertical derivatives (the total of nine DPC signals). From Fig. 4 (d), which shows the error between the model distribution and this integral, it can be seen that the model distribution is determined sufficiently well without influence of noise.

About qDPC Capability

The qDPC [8] is a plug-in for DigitalMicrograph®, and implements the offline capabilities of integrating the DPC signals discussed above. Namely, the qDPC has the following features:

- Functions to create the DPC signal from the signals of a quadrant detector
- Functions to calculate phase distribution by DCT from the DPC signal
- Utilities to correct the DPC signal

In addition, it is possible to evaluate the phase calculated by FFT and the real-time integration routine.

At first, we describe the utilities to correct the DPC signal. Some deficiencies that are not discernible in the DPC signal becomes remarkable when the phase distribution is obtained by integrating the DPC signal. For example, a small adjustment error to the dark level of the segmented detector or misalignment of the transmitted wave on the detector results in a constant imbalance in the DPC signal. Although this imbalance is not visually detectable, it introduces a distinct phase gradient when the DPC signal is integrated. In addition, if an adjustment of the beam deflection system is inaccurate, the transmitted wave moves on the detector according to the beam scanning. When this movement is linear with respect to the scanning position, a slope will appear in the DPC signal. Since a linear function becomes a quadratic function by integration, a slightly inclined plane in the DPC signal may give a remarkable parabolic surface in the integrated phase. Therefore, the qDPC provides the off-line functions of correcting a constant value and/or a constant slope from a DPC signal.

When performing the integration, the coordinate system of the DPC signal, namely the rotation angle of the segmented detector, should coincide with the coordinates of STEM images, namely the scanning system. Also, when displaying electric or magnetic field vectors on a STEM image based on DPC signals, the orientation of the segmented detector should be known in terms of the STEM image coordinate. For this reason, when the segmented detector is installed, the direction of the deflection system is made to match the coordinates of the segmented detector for some camera lengths, or the mutual angle between them is measured and stored as correction data for a later use. In an actual experiment, the operator often rotates the direction of the scanning system, i.e., the STEM image, with respect to the direction of the sample orientation. Therefore, this ad hoc image rotation should be also considered in the relationship between the coordinates of the DPC signal and the image system. Since the rotation adjustment of the DPC signal is so important, the qDPC has the function to determine the rotation angle from the acquired DPC signal

Fig. 4 Phase distribution restored by real-time integration

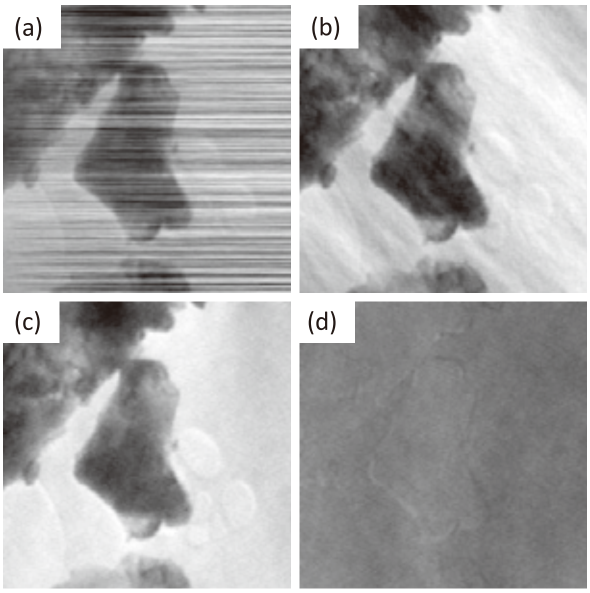

a): The DPC signals are simply added in the scanning direction (horizontal). Pronounced horizontal stripes result from the added noise. (b): The value of a scanning point is obtained by averaging two DPC signals at the directly preceding point and the directly above point. Although weak oblique stripes appear, the restored phase is significantly improved. (c): The value of a scanning point is obtained using four horizontal and five vertical (total of nine) DPC signals in a least-square sense (see text). The error from the model distribution is shown in (d), which demonstrates that the model distribution is obtained without influenced by added noise.

itself. Here, we use the following attribute of integration of the DPC signal: When the relationship between the coordinate systems is correct, the differential of the integration of the DPC signal should reproduce the original DPC signal. Contrary, if the relationship between the coordinate systems is not correct, the integration of the DPC signal will not be performed correctly, and thus the differential of the phase distribution will not reproduce the original DPC signal. Using this property, we rotate the observed DPC signal as a vector, integrate the rotated signal to obtain the phase distribution, and differentiate the phase distribution to obtain an emulated DPC signal. Finally, we calculate the sum of squared difference (SSD) between the emulated and the original DPC signals. Since the differential of the integrated signal returns to the original signal at the correct rotation angle for a noiseless data, the angle that minimizes the SSD would indicate the rotation angle for the real-world data (See **Fig. 6**).

SD module

The qDPC has the optional on-line module, the SD module, where the signals from a segmented detector are acquired in real time using Gatan's DigiScan™ II. Here, the phase distribution is obtained by using the real-time integration routine of the qDPC, and displayed according to the progress of the scan. Since the DigiScan™ II is usually used to capture the BF and/or HAADF signals, we add DigiScan™ II to collect the signals from the segmented detector and transferred them in live to DigitalMicrograph® as shown in **Fig. 5**. In the case of the SAAF Octa, which is a commercial double quadrant detector from JEOL, it is possible to acquire eight signals simultaneously using two DigiScan™ II (Gatan Microscopy Suite® (GMS) 3.4 supports up to four DigiScan™ II). Here, the DPC signals are synthesized from the signals captured into the DigitalMicrograph®, then they are integrated in real time, and a phase distribution is displayed in accord with the scanning (see **Fig. 10**). The phase distribution obtained by real-time integration makes it possible to evaluate the sample and experimental conditions in live mode, and thus we expect the SD module will substantially accelerate the experiment. It is also possible to obtain a more accurate phase distribution by the DCT integration just after the completion of scanning.

4D-STEM module

The qDPC has also another optional extension, the 4D-STEM module, for a pixelated detector. The 4D-STEM module has an offline function that calculates DPC signals from existing 4D-STEM data. Once the DPC signal is obtained from the 4D-STEM data, the phase distribution can be calculated offline using the qDPC function. The 4D-STEM module has also an online function that calculates DPC signals just after the completion of each scan, and obtains the phase distribution in quasi-real-time using the DCT. In the case of the 4DCanvas™, a commercial pixelated detector of JEOL, the DPC signals become available immediately after the completion of scanning, and there is no need to calculate the DPC signal from 4D-STEM data. Therefore, a high-precision phase distribution can be obtained by the DCT integration just after the scanning, which makes it possible to judge the sample and experimental conditions, and thus greatly facilitates the experiment.

Results and Discussion

Up to now, the integration method of the DPC signal has been studied with a model structure. Here, we compare the DCT and FFT integration of the ideal DPC signal, which is obtained as the centroid of the diffraction intensity acquired with a pixelated detector, namely the 4DCanvas™ provided by JEOL. The 4D-STEM data used here is obtained from single-layer graphene observed at 80 kV by 4DCanvas™ attached to a JEOL JEM-ARM200F, and the number of pixels is 256 × 256. Figs. 6 (a) and (b) show the DPC signals (the centroid of the diffraction intensity) calculated from the 4D-STEM data in the camera coordinate system. The DPC signals in (c) and (d) are obtained by rotating the raw DPC signals, (a) and (b), by 31 degrees using the function of the qDPC mentioned above. The phase distributions obtained by the DCT and the FFT-2 using the DPC signal after rotation correction are shown in (e) and (f), respectively. By comparison between the two, it can be seen that the remarkable difference appears in the upper right corner of the phase distributions. In this example, unfortunately multilayer graphene is present at three corners except the upper right of the observation area. Therefore, the periodic boundary condition assumed in the FFT breaks down considerably, and a false image contrast appears at the upper right corner in FFT-

Fig. 5 SD module

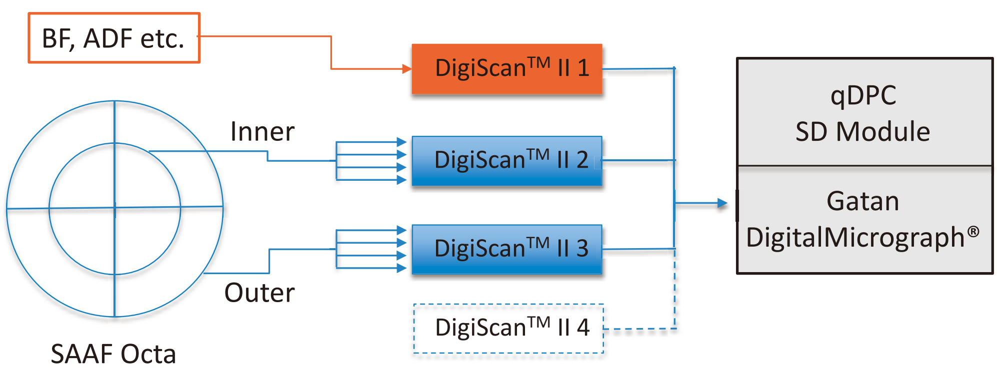

The signals from the segmented detector are taken into DigitalMicrograph® using multiple DigiScan™ IIs (Gatan), and the DPC signals are synthesized. Then, the phase distribution obtained from of the DPC signals by real-time integration is displayed in accord with the scanning. In the case of SAAF Octa, a commercial segmented detector of JEOL, it is possible to acquire eight signals simultaneously using two DigiScan™ II. (See Fig. 10).

2 (consult comparison with Ptychography in **Fig. 9**). Note that a clear six-membered ring like in (e) and (f) does not appear when the phase distribution is obtained from as-acquired DPC signals, (a) and (b).

Next, we compare the phase distributions reconstructed from the emulated DPC signals for the different segmented detectors using the same 4D-STEM data. **Figure 7** (a) and (b) show the phase distributions obtained by DCT from the DPC signals emulated for a quadrant and annular quadrant detectors, respectively. The both phase distributions are very similar to the one shown in Fig. 6 (e) obtained from the DPC signal estimated as the centroid of the diffraction intensity. The histograms of the phase distributions of Fig. 6 (e) and Figs. 7 (a) and (b) are shown in **Figs. 8** (a), (b) and (c), respectively. The histogram (c) obtained from the annular quadrant detector is very similar to the result (a) obtained from the pixelated detector. Figure 8 also shows correlation diagrams of the phase distributions of Figs. 7 (a) and (b) with respect to the phase distribution shown in Fig. 6 (e). The correlation diagram also demonstrates that the phase distribution of Fig. 7 (b) obtained from the annular quadrant detector is very close to the phase distribution of Fig. 6 (e) obtained from the pixelated detector. We may note that the phase change from single-layer graphene has been measured by electron holography as 50 ± 50 mrad [14]. The widths of the main peak of the histograms shown in Fig. 8 (a) and (c) are about 50 mrad, which closely corresponds to the result measured by electron holography. However, an atomic resolution phase distribution as obtained here is not reported in [14]. This seems to be because the DPC is more immune to quantum noise.

Now, the phase distribution obtained by using the DPC signal will be compared with the phase distribution obtained by Ptycography. Figure 9 (a) shows the phase distribution of single-layer graphene obtained by Ptychography from the same 4D-STEM data [15]. The phase distribution of Ptychography is close to the result of the DCT (Fig. 6 (e)), and the abnormal contrast as shown in the result of the FFT (Fig. 6 (f)) does not appear at the upper right. However, the DCT result shows a slight contrast change in the single-layer graphene region, and the contrast of the multilayer graphene regions is slightly different from the Ptychography result. Since the DCT or FFT integration includes a division by frequency during the processing, low frequencies are apt to be emphasized. Figure 9 (b) shows the phase distribution where the low frequency is slightly attenuated from the DCT result, which becomes closer to the one obtained by Ptychography. We have already confirmed that the phase distributions obtained from the DPC signals corresponding to the segmented detectors (Fig. 7) are similar to the phase distribution obtained from the DPC signal estimated from the pixelated detector (Fig. 6 (e)). Therefore, it has been demonstrated that the phase distribution that is used for a practical application can be obtained by integrating the DPC signal from the segmented detector. As introduced in the next section, the phase distribution can be observed in live mode by using the DPC signal from the segmented detector. Contrary, Ptychography is not suitable to obtain the phase distribution in real-time, since it requires a two-dimensional Fourier transform at each diffraction point of the 4D-STEM data [9].

Finally, we will show the SD module applied to JEOL SAAF Octa, where the phase is displayed according to the scan as described in the section for the real time integration method. Figure 10 is a screenshot at the time the SD module is operating, where the sample is STO [$SrTiO_3$]. The upper part

Fig. 6 Phase distributions restored from the DPC signal obtained from the pixelated detector

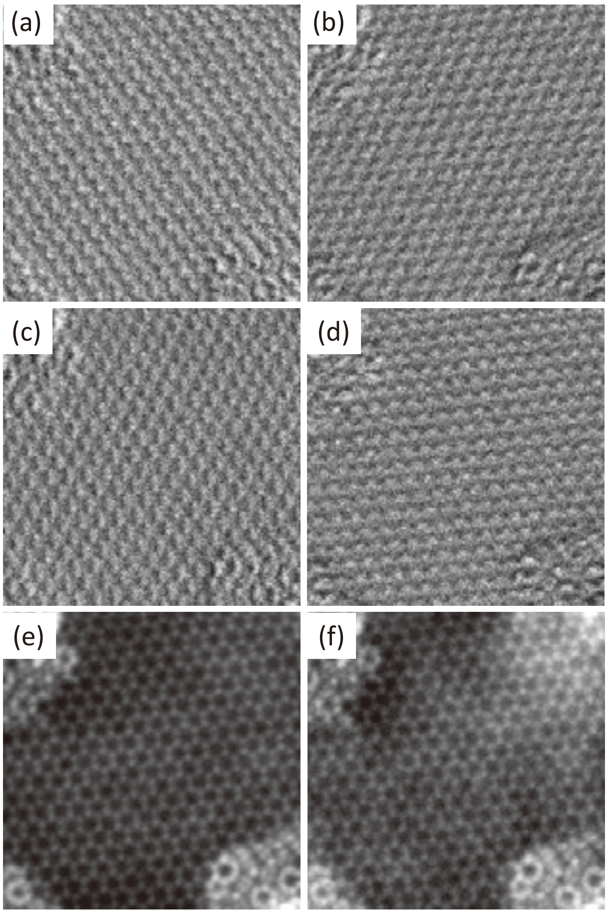

The integration methods were compared using an ideal DPC signal obtained as the centroid of the diffraction intensity of 4D-STEM data. The sample was single-layer graphene, and 4D-STEM data was acquired by 4DCanvas™ mounted on JEM-ARM200F. Top (a and b): DPC signals in two directions calculated from the 4D-STEM data in the camera coordinate system. Middle (c and d): DPC signals in the scanning direction, where the DPC signals are rotated by 31 degrees using the DPC signal correction function. Bottom (e and f): Phase distributions obtained by DCT and FFT-2, respectively, from the rotated DPC signals. A remarkable difference between two phases appears in the upper right, which result from the failure of the periodic boundary condition assumed by FFT (cf. Fig. 9).
Experimental conditions: JEM-ARM200F (acceleration voltage 80 kV, magnification 50M), 4DCanvas™ (264 × 66 pixels (binning 4), 4,000 fps), number of scan points 256 × 256, data acquisition time 16s.

Fig. 7 Phase distributions obtained from the DPC signals emulated for the segmented detectors

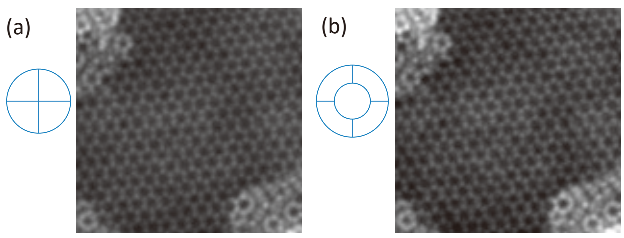

The DPC signals were emulated for a quadrant detector (a) and an annular-quadrant detector (b) from the 4D-STEM data used in Fig. 6. The phase distributions obtained by the DCT from the DPC signals for the quadrant and annular-quadrant detectors are very close to the phase distribution shown in Fig. 6 (e).

displays four signals from the inner or outer quadrant detector, and the lower part from the left corresponds to two synthesized DPC signals, a phase distribution integrated in real time, a simultaneously acquired HAADF image, and an electric field map in color display mode. Although no contrast is visible at the position of oxygen in the HAADF image, contrast from oxygen appears in the DPC signal, phase distribution, and electric field map. The electric field vector here uses the derivative of the phase distribution instead of the observed DPC signal. Therefore, the random noise in this electric field map is reduced compared to the case where the observed DPC signal is displayed. This is because the influence of random noise included in the observed DPC signal is suppressed by the integration as described before. Although this real-time integration can be done in live, the integrated phase is an approximate solution, and does not simultaneously satisfy the entire DPC signal contrary to the solution of the DCT. Nevertheless, the real-time integration will accelerate the experiment significantly, since it gives a sufficiently accurate phase distribution, from which the sample and experimental conditions can be safely evaluated.

Fig. 8 Comparison of phase distributions obtained from the DPC signals of various detectors

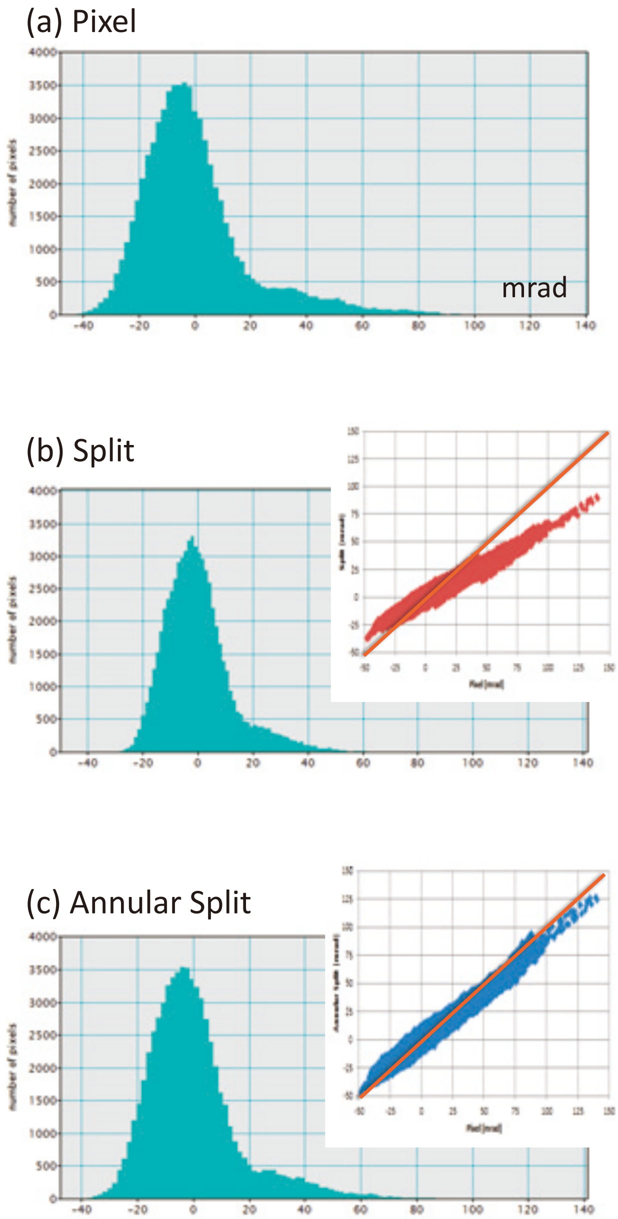

(a): Histogram of the phase distribution of Fig. 6 (e). (b) and (c): Histograms of the phase distributions of Figs. 7 (a) and (b), respectively, where the correlation diagrams with the phase distribution of Fig. 6 (e) are also shown. The histogram and correlation diagram demonstrate that the phase distribution of the annular quadrant detector is close to that of the pixelated detector. The horizontal axis of the phase histogram is mrad.

In Conclusion

Differential phase contrast (DPC) using a two-segment (split) detector has been proposed as a method of observing a phase object in scanning transmission electron microscopy (STEM). From the DPC signal we can obtain the phase distribution, since the DPC signal is a derivative of the phase distribution. In this report, we introduced the discrete cosine transform (DCT) as a method of integration to obtain the phase distribution using the Neumann boundary condition, which is not affected by the boundary of data acquired in a finite interval in contrast to the method based on the fast Fourier transform (FFT) that uses a periodic boundary condition. We also described the real-time integration method that displays the phase in accord with the scanning of the STEM. Then, we examined the phase distributions obtained by DCT from the DPC signals emulated for the segmented detectors using experimental data of single-layer graphene obtained by a pixelated detector, 4DCanvas™. In addition, we compared the phase distribution obtained by DPC with the one obtained by Ptychography, and demonstrated that the segmented detector provides a phase distribution that can be used for a practical application. The phase distribution can be observed in real time by using the DPC signal from a segmented detector, while Ptychography is not suitable for real-time application, since it requires a large

Fig. 9 Comparison of the phase distributions obtained by Ptychography and DPC integration

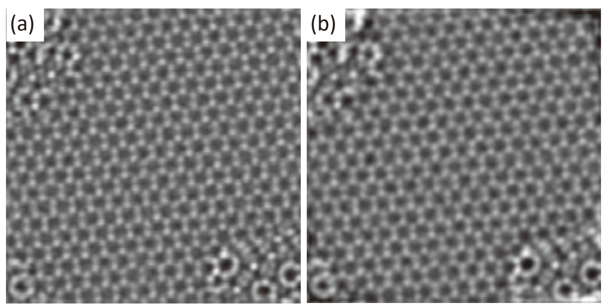

Processed by R. Sagawa (JEOL)

(a): Phase distribution of single-layer graphene obtained by Ptychography. (b): Phase distribution obtained by slightly attenuating low frequencies of Fig. 6 (e). The distribution especially at multilayer graphene regions becomes more similar to (a). This demonstrates that a practically acceptable phase distribution can be obtained using the DPC signal from a segmented detector.

Fig. 10 SD module

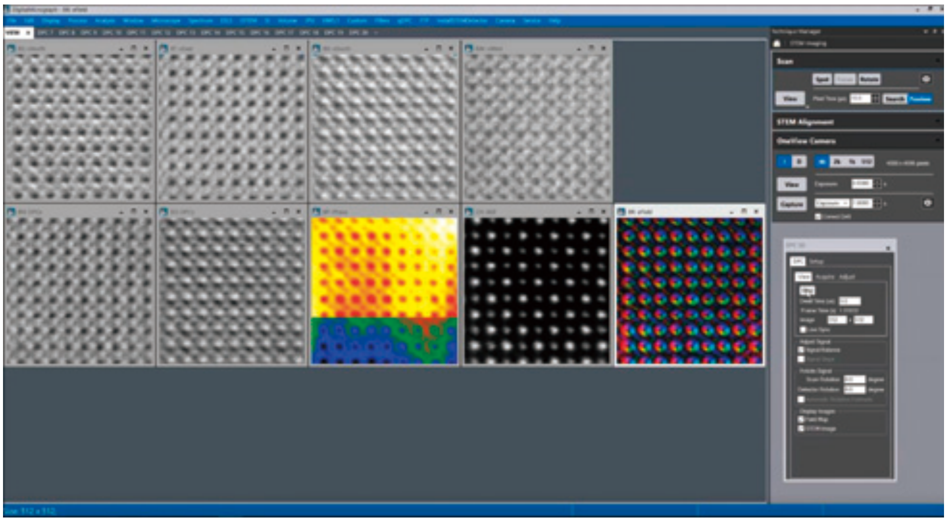

Screenshot showing the SD module in action, where the upper row shows four signals from the inner or outer quadrant detector, while the lower row (from left) shows two synthesized DPC signals, a real-time integrated phase, a HAADF image acquired simultaneously, and an electric field map displayed in color mode. The SD module palette is shown in the right. Pressing the Start button updates these images in accord with the DigiScan™ signal data update. Here, the sample is STO [$SrTiO_3$], and no contrast is seen at the oxygen position in the HAADF image, while some contrast appears in the DPC signal, phase distribution, and electric field map. Since the electric field map here is obtained by differentiating the phase distribution, random noise is reduced compared with the electric field map created by using the observed DPC signal.

amount of calculation. We introduced also the SD module that acquires the signal from a segmented detector, such as SAAF Octa, using Gatan's DigiScan™ II, calculates the DPC signals and displays the phase distribution in live mode. Furthermore, we introduced the 4D-STEM module that displays the phase distribution from the 4D-STEM data in quasi-real-time, namely immediately after the end of scanning. We expect that these online modules will accelerate DPC observation in STEM.

Finally, we have been providing a suite of plug-ins of DigitalMicrograph® (Gatan) for quantitative analysis for electron microscopy. Some of them were introduced in JEOL News [16]. We would be grateful if you could look though it also.

Acknowledgements

The authors would like to express their gratitude to Mr. Onishi and Mr. Okunishi of JEOL for evaluation of the SD module at SAAF Octa, and Mr. Sagawa, Mr. Hashiguchi, and Mr. Yasuhara of JEOL for testing the 4DCanvas™ module. In addition, Mr. Sagawa has kindly provided the raw data of single-layer graphene obtained by 4DCanvas™ and the phase image reconstructed by Ptychography. We also acknowledge JEOL for providing the opportunity to write this article.

References

[1] Okunishi E., Sawada H., and Kondo Y. (2012) Experimental study of annular bright field (ABF) imaging using aberration-corrected scanning transmission electron microscopy (STEM). *Micron*, **43**, 538-544.

[2] Dekkers N. H. and de Lang H. (1974) Differential phase contrast in a STEM. *Optik* **41**, 452-456.

[3] Waddell E.M. and Chapman J.N. (1979) Linear imaging of strong phase objects using asymmetrical detectors in STEM. *Optik* **54**, 83-96.

[4] Rose H. (1977) Nonstandard imaging methods in electron microscopy. *Ultramicroscopy* **2**, 251-267.

[5] Shibata N., Findlay S.D., Kohno Y., et al. (2012) Differential phase-contrast microscopy at atomic resolution. *Nat. Phys*. **8**, 611-615.

[6] Chapman J.N., Batson P.E., Waddell E.M. and Ferrier R.P. (1978) The direct determination of magnetic domain wall profiles by differential phase contrast electron microscopy. *Ultramicroscopy* **3**, 203-214.

[7] McGrouther D., Benitez M-J., McFadzean S., and McVitie S. (2014) Development of Aberration Corrected Differential Phase Contrast (DPC) STEM. *JEOL News* **49**, 2-10.

[8] qDPC, a DigitalMicrograph plug-in: https://www.hremresearch.com/Eng/plugin/qDPCEng.html

[9] Pennycook T.J., Lupini A.R., Yang H., Murfitt M.F., Jones L., Nellist P.D. (2015) Efficient phase contrast imaging in STEM using a pixelated detector. Part 1: Experimental demonstration at atomic resolution. *Ultramicroscopy* **151**, 160–167.

[10] Close R., Chen Z., Shibata N. and Findlay S.D. (2015) Towards quantitative, atomic-resolution reconstruction of the electrostatic potential via differential phase contrast using electrons. *Ultramicroscopy* **159**, 124-137.

[11] Lazic I., Bosch E.G.T and Lazar S. (2016) Phase contrast STEM for thin samples: Integrated differential phase contrast. *Ultramicroscopy* **160**, 265-280.

[12] Press W.H., Teukolsky S.A., Vetterling W.T., Flannery B.P. (1988) Numerical Recipes, Cambridge Univ. Press, Cambridge.

[13] Ishizuka A., Oka M., Seki T., Shibata N., and Ishizuka K. (2017) Boundary-artifact-free determination of potential distribution from differential phase contrast signals. *Microscopy* **66**, 397-405.

[14] Cooper D., Pan CT., and Haigh S. (2014) Atomic resolution electrostatic potential mapping of graphene sheets by off-axis electron holography. *J. of Appl. Physics* **115,** 233709.

[15] Sagawa R. (2017) Development of Pixelated STEM Detector "4DCanvas". *JEOL News* **52**, 53-57.

[16] Ishizuka K. and Okunishi E. (2008) Quantitative Electron Microscopy Using Digital Data Processing. *JEOL News* **43**. 17-22.